




Exploration of trivial and nontrivial electronic phases and of collinear and noncollinear magnetic phases in low-spin d^5 perovskites

Amit Chauhan  and B. R. K. Nanda *

Condensed Matter Theory and Computational Lab, Department of Physics, Indian Institute of Technology Madras, Chennai - 600036, India;
Center for Atomistic Modelling and Materials Design, Indian Institute of Technology Madras, Chennai - 600036, India;
and Functional Oxide Research Group, Indian Institute of Technology Madras, Chennai - 600036, India

 (Received 31 May 2021; revised 4 January 2022; accepted 5 January 2022; published 20 January 2022)

The $4d$ and $5d$ transition metal oxides have become important members of the emerging quantum materials family due to the competition between on-site Coulomb repulsion (U) and spin-orbit coupling (SOC). Specifically, the systems with d^5 electronic configuration in an octahedral environment are found to be capable of possessing invariant semimetallic state and perturbations can lead to diverse magnetic phases. In this work, by formulating a multiband Hubbard model and performing SOC tunable density functional theory+ U calculations on prototypes SrIrO_3 and CaIrO_3 and extending the analysis to other isostructural and isovalent compounds, we present eight quantum phases that can be observed in the family of low-spin d^5 perovskites. In the cubic configuration, the U -SOC phase diagram shows stabilization of nonmagnetic metal phase in the weak U regime irrespective of the strength of SOC with the doubly degenerate t_{2g} - $J_{1/2}$ states occupying the Fermi surface. However, the system become ferromagnetic metal with increasing U while the SOC is maintained low. As the SOC increases, the moderate and higher values of U makes the transition to an antiferromagnetic metal and eventually to an antiferromagnetic insulating state. The GdFeO_3 -type orthorhombic distortion through tilting and rotation of the octahedra reform the t_{2g} states through orbital intermixing to introduce a noncollinear spin arrangement. In the weak correlation regime, the nonmagnetic metal phase transform to ferromagnetic metal phase for weak SOC and an invariant Dirac semimetal phase for the strong SOC. On increasing the correlation strength, the ferromagnetic metal phase becomes insulating while the Dirac semimetal phase becomes a canted antiferromagnetic metal and finally transform to the canted antiferromagnetic insulating phase. Interestingly, in the higher U and higher SOC regimes the normal-spin (S_z) component vanishes to form a pure coplanar spin arrangement. The presence of several soft phase boundaries makes the family of d^5 perovskites an ideal platform to study electronic and magnetic phase transitions under external stimuli.

DOI: [10.1103/PhysRevB.105.045127](https://doi.org/10.1103/PhysRevB.105.045127)

I. INTRODUCTION

In the past decade the discovery that spin-orbit coupling leads to the formation of symmetry protected conducting surface or edge states in a wide range of topological class of compounds, has attracted a great deal of attention among the researchers working in quantum many-body theory [1,2]. Spin-orbit coupling (SOC) is a relativistic effect and it is treated as a small perturbation in solids. But for systems with heavy elements, it varies as fourth power of the atomic number and therefore it has an intriguing influence on the electronic and magnetic structure of such systems. In the family of correlated oxide systems, where the on-site Coulomb repulsion with other competing interactions such as Hund's coupling (J_H), crystal field (Δ) and electron hopping strength (t) create a rich electronic and magnetic phase diagram, the presence of SOC bridges the symmetry protected topologically invariant states and magnetism. Moving down the periodic table from $3d$ to $4d$ to $5d$ elements, while the SOC increases, the d orbitals become more spatially extended to reduce the correla-

tion strength U . For the $5d$ families of oxides, both SOC and U becomes comparable and these two competing interactions give rise to emergent phenomena.

For the experimenters and theoreticians alike, the family of iridates, one of the $5d$ oxide families, have become a test bed for exploring these emergent phenomena that includes the topological Mott insulator [3], fractional Chern insulator [4], Kitaev's celebrated spin liquid phase [5–7], Dirac and Weyl semimetals [8,9], axion insulator [10], and high- T_c superconductivity. For example, pyrochlore iridates exhibit topological semimetal and Mott insulating phases [11–13]. The honeycomb iridates host unconventional magnetic and spin liquid phases [14–18]. The monolayer and bilayer Ruddlesden-Popper strontium iridates, Sr_2IrO_4 and $\text{Sr}_3\text{Ir}_2\text{O}_7$, exhibit canted in-plane and collinear out-of-plane antiferromagnetic (AF) insulating state [19–23].

Among the family of iridates, the orthorhombic perovskite iridates with chemical formula AIrO_3 , constitutes a large class of anisotropic oxides with exceptionally wide range of properties. In these oxides the IrO_6 octahedra is distorted as compared to the symmetric cubic structure. These class of oxides with $Pbnm$ space group symmetry was proposed to realize a new class of metal dubbed topologically crystalline

*nandab@iitm.ac.in

metal with flat surface state and phase transition to other nontrivial phases in the presence of external field has been theoretically proposed [24]. For example, SrIrO₃ and CaIrO₃ are paramagnetic Dirac semimetals (DSM) [25–28]. Carter *et al.* [29] showed that SrIrO₃ undergoes a phase transition from semimetal to strong topological insulator by breaking the mirror symmetry. BaIrO₃ is a Pauli paramagnetic metal with Fermi liquid ground state below 6 K [30]. In comparison to the AIrO₃, the other 3*d* and 4*d* perovskites with isovalent *d*⁵ configuration, where the SOC is weak and electron correlation is strong, have different electronic and magnetic phases in their ground state. For example, SrCoO₃ and CaCoO₃ exhibits a high-spin ferromagnetic metal (FM) state whereas SrRhO₃ and YRuO₃ exhibits low-spin (LS) FM and a canted antiferromagnetic insulator (CAFI) ground state [31–34].

For the perovskites, due to strong octahedral crystal field the *d* orbital degeneracy gets lifted giving rise to a *t*_{2*g*} and *e*_g manifold. In the presence of SOC the *t*_{2*g*} manifold splits into spin-orbital entangled pseudospin $J_{\text{eff}} = 3/2$ and $J_{\text{eff}} = 1/2$ states. In the case of a *d*⁵ (Ir⁴⁺) configuration, the $J_{\text{eff}} = 3/2$ states are completely occupied and the ground state is constituted of the $J_{\text{eff}} = 1/2$ pseudospin. These narrow $J_{\text{eff}} = 1/2$ bands formed due to strong SOC are more susceptible to Mott localization by *U*, due to reduced bandwidth, which implies that stronger the SOC is, weak critical *U* (*U*_c) will be required to make a transition from metal to a spin-orbit coupled Mott insulator. By carrying out first-principles density functional theory (DFT) calculations within the framework of local density approximation (LDA)+*U* on the prototype system SrIrO₃, Zeb *et al.* [35] presented an electronic phase diagram in the *U*-SOC configuration space, and broadly suggested three domains. These are magnetic metals in the weak to intermediate SOC and weak to high *U* regime, nonmagnetic metal (NM) or DSM in the weak to intermediate *U* and weak to high SOC regime, and magnetic insulator in the weak to high SOC and intermediate to high *U* regime.

The aforementioned discussion on the electronic structure of orthorhombic perovskites suggest that a much more intricate phase diagram needs to be constructed for the family of *d*⁵ oxides in the *U*-SOC space in order to explore the emerging quantum phases in this family. Firstly, it needs to be revisited if in the absence of SOC, the system remains metallic even for very high *U*. Secondly, in the absence of collinear spin arrangement questions arise whether subdomains with nontrivial quantum states exist within the four proposed broad domains. Thirdly, the role of structural distortions — from the isotropic cubic configuration to symmetry lowered orthorhombic configuration — needs to be examined in building the phase diagram as it is known to be a key player in driving the electronic and magnetic phase transitions in the perovskite family [36–43].

In this work we have employed a multiband Hubbard model which is solved self-consistently in the mean-field framework and validated the results with DFT+*U* calculations to establish a detailed phase diagram discovering the earlier unexplored subdomains. The present study establishes the complex interplay among SOC, *U*, Δ and structural distortions to explain the formation of collinear and noncollinear magnetism as well as metallic, insulating, and nontrivial semimetallic phases in the family of LS *d*⁵ perovskites.

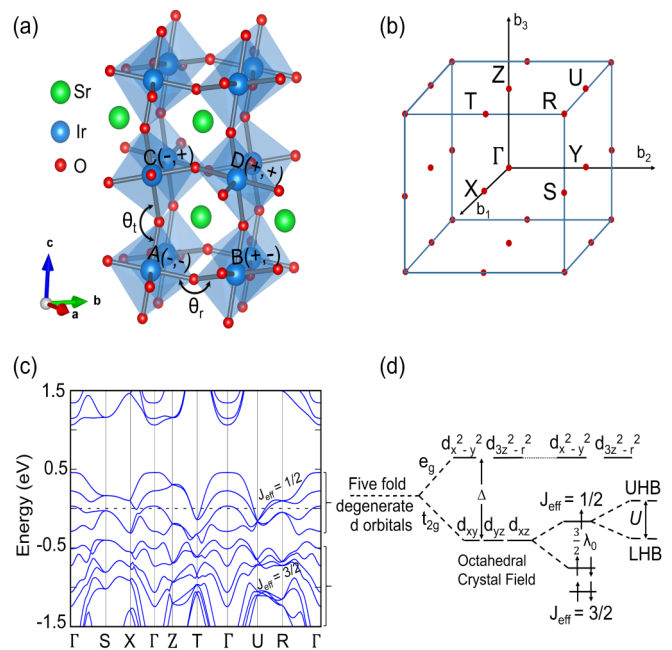


FIG. 1. (a) Crystal structure of orthorhombic SrIrO₃. (b) Corresponding bulk Brillouin zone with high symmetric *k* points. (c) Bulk electronic structure of SrIrO₃ obtained using DFT+*U* with $U_{\text{eff}} = 0$ and $\lambda/\lambda_0 = 1$. Here, λ_0 is the real SOC strength with magnitude 0.43 eV, respectively. The Fermi level is set to be 0. A Dirac node appears at the high symmetric *k* point *U* revealing the semimetallic nature of SrIrO₃. (d) Schematic illustration of the effect of crystal field, SOC and on-site Coulomb repulsion on the Ir-*d* states.

II. STRUCTURAL AND COMPUTATIONAL DETAILS

Bulk SrIrO₃ crystallizes in an orthorhombic perovskite crystal structure (space group *Pbnm*) with the GdFeO₃-type lattice distortion as shown in Fig. 1(a). The IrO₆ octahedra undergoes a staggered rotation about the *c* axis by an angle $\theta_r = 153.53^\circ$, followed by another rotation about the [110] direction by tilt angle $\theta_t = 156.52^\circ$. Due to these tilt and rotations of the IrO₆ octahedra, the unit cell gets doubled in the *ab* as well as in the *ac* plane due to $\sqrt{2}a_0 \times \sqrt{2}a_0 \times 2a_0$ supercell geometry where *a*₀ is the nearest-neighbor (NN) Ir-Ir distance. Hence, SrIrO₃ contains four formula units per unit cell leading to four inequivalent Ir sublattices (A,B,C,D). The two signs on each Ir sublattice represents the sense of the rotation and tilting of the octahedra, clockwise (+) or anticlockwise (−). The experimental lattice parameters are *a* = 5.56 Å, *b* = 5.59 Å, and *c* = 7.88 Å [44]. In order to study the effect of correlation and SOC on the electronic and magnetic phases in bulk SrIrO₃, we developed a multiband Hubbard model and solved it self-consistently as discussed in Sec. IV and also carried out comprehensive DFT calculations in the *U*-SOC space. The calculations are performed using plane-wave based projector augmented wave (PAW) method [45,46] as implemented in Vienna *ab initio* simulation package (VASP) [47] within the Perdew-Burke – Ernzerhof generalized gradient approximation for exchange-correlation functional. In this study, the SOC λ is varied in units of λ_0 , where λ_0 is the real SOC strength (=0.43 eV) as obtained from the self-consistent field calculations to achieve

the ground state. The Brillouin zone integrations are carried out using $8 \times 8 \times 4$ Monkhorost-Pack k mesh which yields 256 k points in the irreducible part of the Brillouin zone. The kinetic energy cutoff for plane-wave basis set was chosen to be 500 eV. The strong correlation effect is incorporated via an effective on-site correlation parameter $U_{\text{eff}} = U - J$ through the rotationally invariant approach introduced by Dudarev [48].

III. GROUND STATE ELECTRONIC STRUCTURE OF SrIrO₃

The ground state electronic structure, as shown in Fig. 1(c), implies that bulk SrIrO₃ exhibits nonmagnetic semimetallic ground state with a Dirac node at the high symmetry point U . This is due to the combined effect of cubic asymmetry, octahedral crystal field, and SOC towards the removal of degeneracy in the d manifold as illustrated in Fig. 1(d). Due to a strong octahedral crystal field, the fivefold degenerate d states split into a higher-energy and unoccupied e_g doublet and a lower-energy t_{2g} triplet. While the e_g states are unaffected by the SOC, the t_{2g} manifold is further SOC split into a $J_{\text{eff}} = 1/2$ doublet ($m_j = \pm 1/2$) and a $J_{\text{eff}} = 3/2$ ($m_j = \pm 3/2, \pm 1/2$) quartet, hence, forming three Kramer's pair. The expressions $|J, m_j\rangle$ are given by

$$\left| \frac{1}{2}, \pm \frac{1}{2} \right\rangle = \frac{1}{\sqrt{3}} (|yz, \bar{\sigma}\rangle \pm |xy, \sigma\rangle \pm i |xz, \bar{\sigma}\rangle), \quad (1)$$

$$\left| \frac{3}{2}, \pm \frac{1}{2} \right\rangle = \frac{1}{\sqrt{6}} (|yz, \bar{\sigma}\rangle \mp 2|xy, \sigma\rangle \pm i |xz, \bar{\sigma}\rangle), \quad (2)$$

$$\left| \frac{3}{2}, \pm \frac{3}{2} \right\rangle = \frac{1}{\sqrt{2}} (|yz, \sigma\rangle \pm i |xz, \sigma\rangle), \quad (3)$$

where \pm corresponds to spin $\sigma = \uparrow/\downarrow$, respectively. With lowering in symmetry through θ_r and θ_t , two pairs of bands make a linear crossing at the high symmetry point U to create double Dirac nodes resulting in a DSM phase. It has been reported that the two Dirac nodes may not be degenerate in energy and in that case the cones may penetrate to form a nodal ring [35]. Through our model Hamiltonian in Sec. IV, we will attribute the formation of the DSM phase due to the development of t_{2g} - e_g interaction in the next-nearest neighborhood (NNN) due to tilting and rotation of octahedra. Besides the crystal field and SOC, the on-site Coulomb repulsion is also deterministic of the electronic structure of the d^5 (Ir^{4+}) compounds. Four out of five d electrons occupy the $J_{\text{eff}} = 3/2$ state, leaving one electron in the $J_{\text{eff}} = 1/2$ state [see Fig. 1(d)]. The on-site repulsion further splits this degenerate state to create a lower Hubbard (LHB) and upper Hubbard (UHB) subband. However, experimental studies [25,26,49] including angle-resolved photoemission spectroscopy measurements show that the SrIrO₃ is a paramagnetic semimetal. This demonstrates that the competition between SOC and U can lead to a plethora of electronic and magnetic phases for the d^5 perovskites.

Apart from the perovskite structure, several other iridates and iridatlike systems with d^5 configuration and with similar octahedral complexes, exhibit a wide range of magnetic phases with spin anisotropy [16,19,50–53]. Therefore, we utilize SrIrO₃ as a prototype to build a platform so that the

emerging quantum phases in the U -SOC configuration space can be envisaged and analyzed. The phase diagram will be discussed in detail in Sec. V.

IV. MULTIBAND HUBBARD MODEL

Across the iridates family, it has been shown that the competition between U and λ influences the eigen states substantially. To get a flavor of it in the single perovskite structure, we employ a mean-field based multiband Hubbard model Hamiltonian to explore the nontrivial/trivial phases emerging in the weak/strong U -SOC regime. To start with, we first consider a tight binding (TB) model with SOC, where a minimal basis set formed by Ir- d orbitals ($xy, yz, xz, x^2 - y^2, 3z^2 - r^2$) has been considered. The five orbital basis set, instead of t_{2g} based three orbital, introduces t_{2g} - e_g intermixing due to finite θ_r and θ_t in the distorted frame leading to significant altering of the band structure.

To extract the NN, NNN σ and π hopping interactions and SOC strength, a TB model for undistorted SrIrO₃ is formulated and then using these parameters and transforming the hopping matrices in the rotated basis (as explained in Appendix A), the effect of distortion on the electronic and magnetic properties has been examined. In the second quantization notation, the TB + SOC component of the Hamiltonian is given by

$$\begin{aligned} H_{\text{TB-SOC}} = & \sum_{i,\alpha} \epsilon_{i,\alpha} c_{i,\alpha}^\dagger c_{i,\alpha} \\ & + \sum_{i,j,\alpha,\beta,\sigma} t_{i,\alpha,j,\beta} (c_{i,\alpha}^\dagger c_{j,\sigma,\beta} + \text{h.c.}) \\ & + \lambda \sum_{\alpha,\beta,\sigma,\bar{\sigma}} \langle \alpha\sigma | \mathbf{L} \cdot \mathbf{S} | \beta\bar{\sigma} \rangle c_{\alpha,\sigma}^\dagger c_{\beta,\bar{\sigma}} \end{aligned} \quad (4)$$

Here, $i(j)$, $\alpha(\beta)$ are site and orbital indices, respectively. The parameters $\epsilon_{i\alpha}$ and $t_{i\alpha j\beta}$ represents the on-site energy and strength of hopping integrals, respectively. The SOC is added in the third term of the Hamiltonian with λ denoting its strength. In compact form, for a single formula unit as is the case with cubic perovskite structure, H is given by

$$H = \begin{pmatrix} H_{\uparrow\uparrow}^{5 \times 5} & H_{\uparrow\downarrow}^{5 \times 5} \\ H_{\downarrow\uparrow}^{5 \times 5} & H_{\downarrow\downarrow}^{5 \times 5} \end{pmatrix}. \quad (5)$$

Here, $H_{\uparrow\uparrow} = H_{\downarrow\downarrow}$ and $H_{\uparrow\downarrow} = (H_{\downarrow\uparrow})^\dagger$ to ensure the time reversal (TR) invariance of the Hamiltonian. For the four formula unit ($\sqrt{2}a_0 \times \sqrt{2}a_0 \times 2a_0$) supercell, which builds the primitive unit cell of the orthorhombic phase, the augmented Hamiltonian representing four-Ir (A,B,C,D) sublattices then takes the shape of

$$H = \begin{pmatrix} H_{\uparrow\uparrow}^{20 \times 20} & H_{\uparrow\downarrow}^{20 \times 20} \\ H_{\downarrow\uparrow}^{20 \times 20} & H_{\downarrow\downarrow}^{20 \times 20} \end{pmatrix}. \quad (6)$$

The TB component built with Slater-Koster formalism [54] is further elaborated in Appendix A.

For the distorted case, with finite θ_r and θ_t , as defined through Fig. 1(a), the hopping matrices are obtained by using the following transformation:

$$\tilde{H}_{\text{TB}} = R^T H_{\text{TB}} R, \quad (7)$$

where R is the transformation matrix and can be calculated using rotation matrix for the cubic harmonics ($L = 2$)

$$R(\theta_t) = \begin{pmatrix} \frac{1}{2}(1 + \cos^2 \theta_t) & \frac{1}{2\sqrt{2}} \sin 2\theta_t & -\frac{1}{2\sqrt{2}} \sin 2\theta_t & 0 & -\sqrt{\frac{3}{4}} \sin^2 \theta_t \\ -\frac{1}{2\sqrt{2}} \sin 2\theta_t & \frac{1}{2}(2 \cos^2 \theta_t + \cos \theta_t - 1) & -\frac{1}{2}(2 \cos^2 \theta_t - \cos \theta_t - 1) & -\frac{1}{\sqrt{2}} \sin \theta_t & -\sqrt{\frac{3}{8}} \sin 2\theta_t \\ \frac{1}{2\sqrt{2}} \sin 2\theta_t & -\frac{1}{2}(2 \cos^2 \theta_t - \cos \theta_t - 1) & \frac{1}{2}(2 \cos^2 \theta_t + \cos \theta_t - 1) & -\frac{1}{\sqrt{2}} \sin \theta_t & \sqrt{\frac{3}{8}} \sin 2\theta_t \\ 0 & \frac{1}{\sqrt{2}} \sin \theta_t & \frac{1}{\sqrt{2}} \sin \theta_t & \cos \theta_t & 0 \\ -\sqrt{\frac{3}{4}} \sin^2 \theta_t & \sqrt{\frac{3}{8}} \sin 2\theta_t & -\sqrt{\frac{3}{8}} \sin 2\theta_t & 0 & 1 - \frac{3}{2} \sin^2 \theta_t \end{pmatrix}. \quad (8)$$

$$R(\theta_r) = \begin{pmatrix} \cos 2\theta_r & 0 & 0 & \sin 2\theta_r & 0 \\ 0 & \cos \theta_r & \sin \theta_r & 0 & 0 \\ 0 & -\sin \theta_r & \cos \theta_r & 0 & 0 \\ -\sin 2\theta_r & 0 & 0 & \cos 2\theta_r & 0 \\ 0 & 0 & 0 & 0 & 1 \end{pmatrix}. \quad (9)$$

The values of the on-site energy (ϵ), hopping strength (t) and SOC strength (λ_0) are obtained by fitting the TB+SOC bands with the DFT+SOC bands for the undistorted case as shown in Figs. 2(a) and 2(b). The fitted values are listed in Table I. TB bands, as shown in Fig. 2, capture very well the essential features of the DFT band structure. In this LS ($t_{2g}^5 e_g^0$) configuration, while the overlapping of the t_{2g} and e_g bands is prominent in the undistorted frame [Figs. 2(a) and 2(b)], they are very well segregated in the distorted frame [Fig. 2(c)] and this is very well captured in our TB model [Fig. 2(d)]. The distortion also introduces a DSM phase as linear bands cross each other at the high symmetry point U in the vicinity of the Fermi energy (E_F).

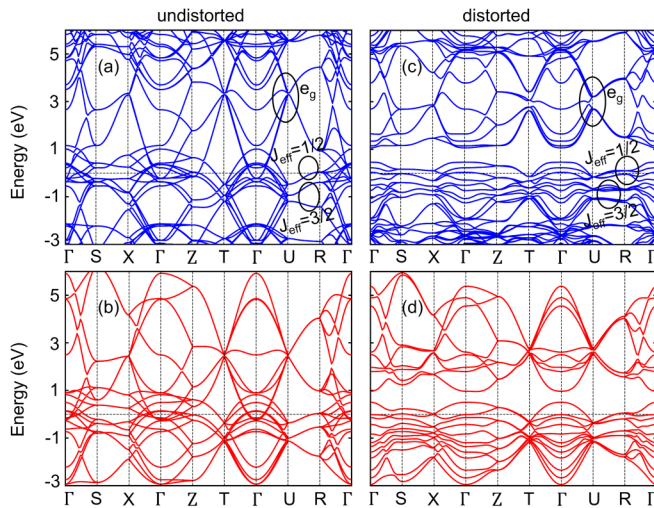


FIG. 2. DFT (blue) and TB (red) band structures for undistorted (a),(b) and distorted (c),(d) SrIrO₃ with $\lambda = 0.43$ eV, respectively. Segregation of t_{2g} and e_g states, as well as the formation of DSM phase, due to distortion of the octahedra.

[Eq. (A3) of Appendix A]. For the rotation and tilting, as appropriate for SrIrO₃, it is, respectively, defined as

Having formulated the kinetic part of the Hamiltonian, we now consider the interacting part of the Hamiltonian (H_{int}) which is described in terms of the multiorbital Hubbard-Kanamori formalism [55]:

$$H_{\text{int}} = U \sum_{i,\alpha} n_{i,\alpha,\uparrow} n_{i,\alpha,\downarrow} + \left(U' - \frac{J_H}{2} \right) \sum_{i,\alpha < \beta} n_{i,\alpha} n_{i,\beta} - 2J_H \sum_{i,\alpha < \beta} S_{i,\alpha}^z \cdot S_{i,\beta}^z = H_1 + H_2 + H_3. \quad (10)$$

Here, the first two terms gives the energy cost of having the electrons in the same or different orbitals at the same lattice site. The third term defines the Hund's rule coupling that favors the ferromagnetic alignment of spins in the orbitals at the same lattice site. The relation $U' = U - 2J_H$ between the Kanamori parameters [56] has been used here.

In the Hartree approximation, H_1 , H_2 , and H_3 can be decoupled as

$$H_1 \approx U \sum_{i,\alpha} (n_{i,\alpha,\uparrow} \langle n_{i,\alpha,\downarrow} \rangle + n_{i,\alpha,\downarrow} \langle n_{i,\alpha,\uparrow} \rangle - \langle n_{i,\alpha,\downarrow} \rangle \langle n_{i,\alpha,\uparrow} \rangle), \quad (11)$$

$$H_2 \approx U \sum_{i,\alpha < \beta} (n_{i,\alpha} \langle n_{i,\beta} \rangle + n_{i,\beta} \langle n_{i,\alpha} \rangle - \langle n_{i,\alpha} \rangle \langle n_{i,\beta} \rangle), \quad (12)$$

$$H_3 \approx -\frac{J_H}{2} \sum_{i,\alpha < \beta} (n_{i,\alpha,\uparrow} \langle n_{i,\beta,\uparrow} \rangle + n_{i,\beta,\uparrow} \langle n_{i,\alpha,\uparrow} \rangle - n_{i,\alpha,\uparrow} \langle n_{i,\beta,\downarrow} \rangle - n_{i,\beta,\downarrow} \langle n_{i,\alpha,\uparrow} \rangle - n_{i,\alpha,\downarrow} \langle n_{i,\beta,\uparrow} \rangle - n_{i,\beta,\uparrow} \langle n_{i,\alpha,\downarrow} \rangle + n_{i,\alpha,\downarrow} \langle n_{i,\beta,\downarrow} \rangle + n_{i,\beta,\downarrow} \langle n_{i,\alpha,\downarrow} \rangle - \langle n_{i,\alpha,\uparrow} \rangle \langle n_{i,\beta,\uparrow} \rangle + \langle n_{i,\alpha,\uparrow} \rangle \langle n_{i,\beta,\downarrow} \rangle + \langle n_{i,\alpha,\downarrow} \rangle \langle n_{i,\beta,\uparrow} \rangle - \langle n_{i,\beta,\downarrow} \rangle \langle n_{i,\alpha,\downarrow} \rangle), \quad (13)$$

TABLE I. Calculated values of on-site energy, interaction parameters and SOC strength in units of eV. The parameters ϵ_1 and ϵ_2 give the values of onsite energy for t_{2g} and e_g states, respectively. For the undistorted case, we have considered identical hopping strengths, t_1 (NN π), t_2 (NNN σ) and t_3 (NNN π) for $t_{2g} - t_{2g}$ interactions, t_4 (NN σ), t_5 (NNN σ), t_6 (NNN π) for $e_g - e_g$ interactions and t_7 (NNN σ) for $t_{2g} - e_g$ interactions, as relevant for the cubic symmetry.

ϵ_1	ϵ_2	t_1	t_2	t_3	t_4	t_5	t_6	t_7	λ
-0.79	2.4	-0.38	-0.13	0.04	-0.85	-0.5	0.1	0.04	0.43

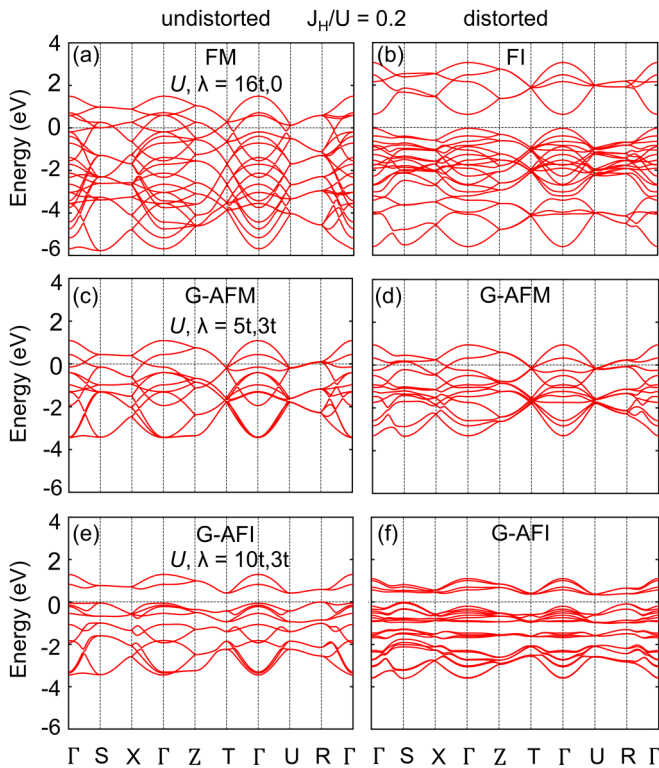


FIG. 3. Electronic band structures obtained for the undistorted structure (first column) and for the distorted structure (second column) with $t = 0.38$ eV defined as the energy scale unit. (a),(b) without SOC and high U , (c),(d) with SOC and low U , and (e),(f) with SOC and moderate U value.

where, $n_{i,\alpha} = n_{i,\alpha,\uparrow} + n_{i,\alpha,\downarrow}$, is the total charge density of orbital α at site i .

Hence, the total Hamiltonian is given by

$$H = H_{\text{TB-SOC}} + H_{\text{int}}. \quad (14)$$

It is solved self-consistently in the momentum space by employing the Hartree approximation as described above. The U -SOC space give rise to different magnetic phases, as shown in Fig. 3, beyond the semimetallic nonmagnetic phase. We set $J_H/U = 0.2$ as relevant for $4d/5d$ oxides [57] and $t = t_1$ as the energy scale unit. For $\lambda = 0$, a FM phase [see Fig. 3(a)], with highly dispersive bands (higher mobility) stabilizes. For even higher U values, a FM state remains stable for the undistorted case.

With SOC, the system shows intriguing magnetic phases where the $J_{\text{eff}} = 1/2$ states determine the ground state. For lower U values, a weak G -type antiferromagnetic metal (G-AFM) state [Fig. 3(c)] with broken Dirac node forms the ground state. It is due to breaking of the TR symmetry. Here, the SOC induces the spin degeneracy and strengthens the localization and hence decreases the mobility. The weak G-AFM state has small hole and electron pockets which disappears on further increasing U and a gap is opened in the $J_{\text{eff}} = 1/2$ spectrum to stabilize a G -type antiferromagnetic insulator (G-AFI) phase [Fig. 3(e)]. Finite distortion induces anisotropy in the orbital (t_{2g}) occupancies with onsite Coulomb repulsion enhances the spin split and drives the system to a ferromagnetic insulator (FI) phase [Fig. 3(b)]. Hence,

competition between U , SOC and structural distortion alters the magnetic and electronic phase of the system substantially. Recent studies on iridates and their superlattices emphasize the crucial role of distortion induced anisotropic spin interactions leading to noncollinear magnetic phases [42,43,58]. However, the current model is based on collinear magnetism and therefore cannot predict noncollinear phases due to the absence of exchange terms in the Hamiltonian. Therefore, we carried out pseudopotential based DFT calculations to explore the novel electronic and magnetic states in the U -SOC domain and build the quantum phase diagram of d^5 perovskites in the LS state by taking SrIrO_3 as a prototype.

V. DFT+ U +SOC ELECTRONIC STRUCTURE

Through Fig. 4, we will analyze the electronic structure evolution as a function of U and SOC. In the ground state, we estimated the SOC strength λ_0 to be 0.43 eV by measuring the split between $J_{\text{eff}} = 1/2$ and $J_{\text{eff}} = 3/2$ states which is equal to $3/2 \lambda_0$ [see Fig. 1(d)]. In order to examine the role of λ , we scaled it in units of λ_0 . For $\lambda/\lambda_0 = U_{\text{eff}} = 0$, it is a pure octahedral crystal field effect where the d orbitals split into lower-lying and partially occupied threefold degenerate t_{2g} and upper-lying twofold degenerate e_g states as shown in Figs. 4(a) and 4(b). Due to imbalance in the population of the states in two different spin channels the system becomes a Stoner ferromagnet. As λ/λ_0 increases, real spin states of the t_{2g} manifold evolve and give rise to pseudospin states with the formation of spin-orbit entangled $J_{\text{eff}} = 1/2$ states lying in the vicinity of the E_F and $J_{\text{eff}} = 3/2$ states lying below in the valence band. For weak λ/λ_0 , the four $J_{\text{eff}} = 1/2$ pairs, corresponding to the four-Ir sublattices, create two set of fourfold degenerate bands along the k path U - R . These two sets merge at the high symmetry point U with increasing SOC to form a DSM phase [see Figs. 4(e), 4(g) and 4(i)].

With increasing correlation effect, say for $U_{\text{eff}} = 3$ eV and no SOC, as shown in Figs. 4(c) and 4(d), the on-site repulsion $U_{n_\uparrow n_\downarrow}$ increases the spin split to form a gap which in turn makes the system a FI. This phase is very well captured by the model Hamiltonian described in the previous section. As SOC competes with U , Figs. 4(f), 4(h) and, 4(j), the four $J_{\text{eff}} = 1/2$ pairs create lower and upper Hubbard subbands, which breaks the Dirac node to form a gap and concurrently stabilizes the system in a CAFI state. The band gap rises from 0.23 eV at $\lambda/\lambda_0 = 0$ to 0.93 eV at $\lambda/\lambda_0 = 2$, manifesting the amplified effect of correlations as the SOC strength increases. The spin anisotropy and the overall phases predicted in the U -SOC domain will be elaborated further in the next subsection.

Bulk phase diagram

The phase diagram for the orthorhombic SrIrO_3 spanned in U -SOC space, as evaluated from the DFT+ U +SOC calculations is presented in Fig. 5. It shows five distinct phases: (i) collinear FM as shown in blue, (ii) collinear FI as shown in maroon, (iii) canted antiferromagnetic semimetal (CAFS) as shown in grey, (iv) CAFI as shown in red, and (v) DSM as shown in green. Let us first examine the weak SOC regime ($\lambda/\lambda_0 \leq 0.2$). Up to $U_{\text{eff}} \approx 2.5$ eV, the system remains a FM with collinear magnetic ordering as shown in Fig. 6(a).

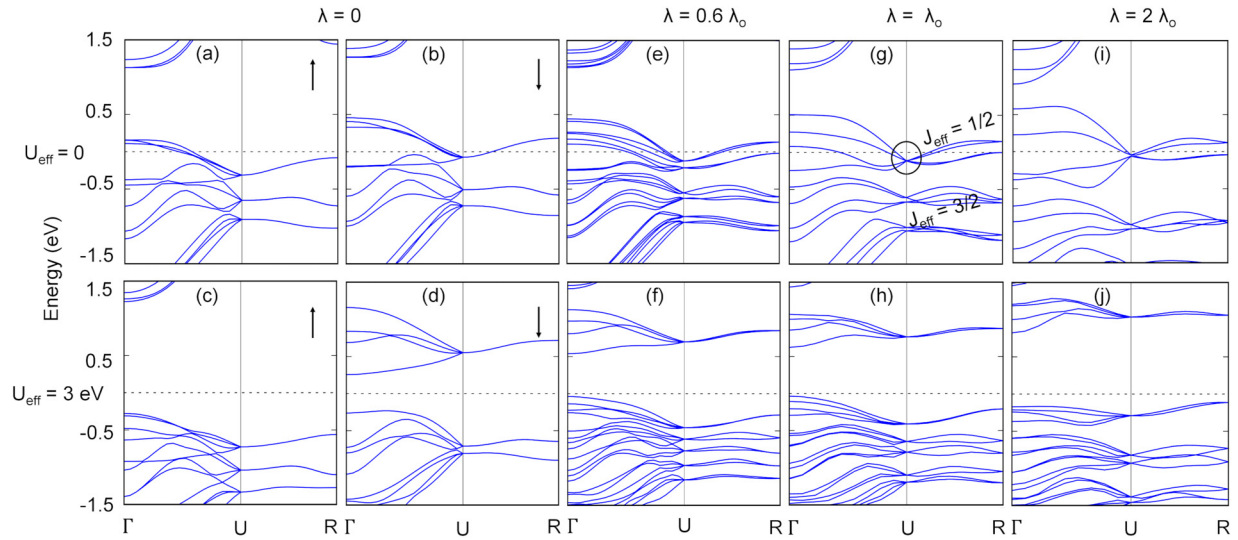


FIG. 4. Evolution of bulk electronic structure as a function of U_{eff} and SOC. The upper and lower rows represent the band structure without and with U_{eff} for four values of λ/λ_0 , namely, 0 (a)–(d), 0.6 (e), (f), 1 (g), (h), and 2 (i), (j). (Upper row) Mixing of up-spin and down-spin states with increasing λ/λ_0 leading to the formation of DSM phase. (Lower row) Amplified effect of correlations with increasing λ/λ_0 . Enhanced spin splitting leads to a gap opening and stabilizes the system in a ferromagnetic insulator state for $\lambda = 0$ and in a canted antiferromagnetic insulator state for finite λ/λ_0 .

This results from the imbalance of the population of partially occupied t_{2g} states in the up-spin and down-spin channels as already explained through Figs. 4(a) and 4(b) in the previous subsection. With further increase in U , the system undergoes a transition from FM to FI because of the fact that with enhanced spin split the earlier partially occupied band in the up-spin channel is now occupied completely whereas in the down spin channel it becomes empty [see Figs. 4(c) and 4(d)]. The FI phase, as predicted from our model and DFT calculations, was not captured in the earlier study [35] where the stability of the metallic phase for all U in the non-SOC regime was reported. It may be noted that the authors there have carried out the calculations using the full-potential linearized augmented-plane-wave method with LDA exchange-correlation functional. The strength of the local magnetic moment at Ir depends on U_{eff} . It increases from $0.27 \mu_B$ at $U_{\text{eff}} = 0$ eV to $0.72 \mu_B$ at $U_{\text{eff}} = 4$ eV. With the LS state, the saturated magnetic moment is $1 \mu_B$ which can be realized for a further higher value of U . The LS state favors the ferromagnetic order over the antiferromagnetic one.

With finite λ/λ_0 , the up-spin and down-spin states mix to form spin-orbit entangled pseudospin $J_{\text{eff}} = 1/2$ and $J_{\text{eff}} = 3/2$ states. The former occupy the E_F and hence determine the electronic and magnetic phase of the system. For the intermediate range ($0.4 \leq \lambda/\lambda_0 \leq 1.4$), the lower value of U_{eff} maintains the metallicity and at the same time weakens the magnetic state with the formation of a DSM phase. It is important to note that the electron hopping, SOC and on-site Coulomb repulsion are in the same energy scale and hence any perturbation can give rise to a different quantum phase. Here, we show that even weak U_{eff} transforms the DSM to CAFS phase suggesting this weakly correlated perovskite is near to the magnetic instability. The on-site Coulomb repulsion facilitates the noncollinear ordering of the spin-orbit entangled states as the planar-spin (S_p) component increases in magnitude in proportion to λ/λ_0 which can be observed from the

spin-intensity map shown in the middle panel of Fig. 5. The on-site repulsion also strengthens the localization to stabilize the CAFI phase as can be seen from the phase diagram.

For the large λ/λ_0 regime ($\lambda/\lambda_0 \geq 1.4$), the system exhibits either DSM for low U or CAFI phase for lower and higher U_{eff} values. In the latter case, the S_z component gradually vanishes with SOC (see Fig. 5 middle panel) to create a transition from the collinear along z to non-coplanar and canted to pure co-planar spin arrangement. This transition is schematically illustrated in Fig. 6. Earlier studies have presented an unusual trend where it has been suggested that higher value of U_{eff} is required to induce metal-to-insulator transition for the higher value of SOC [35]. However, as expected, in this study we observe that a lower U_{eff} value is sufficient to stabilize a CAFI phase.

The $4d$ perovskites SrRhO_3 , LaRuO_3 , and YRuO_3 and the $5d$ perovskites are reported to be having LS d^5 electronic configuration and all of them undergo GdFeO_3 -type distortion of varied order. Their electronic and magnetic phases can be mapped to the phase diagram of Fig. 5. The compounds SrRhO_3 [33] and LaRuO_3 [59], with weak SOC and moderate correlation exhibits FM ground state and can be placed in the region ($0.2 \leq \lambda/\lambda_0 \leq 0.4$, $1 \leq U_{\text{eff}} \leq 2$ eV). The compound YRuO_3 [34] exhibits CAFI phase and lies in the ($0.6 \leq \lambda/\lambda_0 \leq 0.8$, $3 \leq U_{\text{eff}} \leq 4$ eV) zone. Like SrIrO_3 , CaIrO_3 [27] stabilizes in nonmagnetic DSM phase and lies in the ($0.8 \leq \lambda/\lambda_0 \leq 1$, $0 \leq U_{\text{eff}} \leq 0.5$ eV) zone of the phase diagram. In Appendix C, we have compared the phase diagrams of SrIrO_3 and CaIrO_3 (see Fig. 11) to demonstrate the generality of the electronic structure evolving out of competition between electron-electron correlation and SOC.

To identify the division of role between SOC and structural distortions in establishing quantum phases, here, we have computed the phase diagram for undistorted (cubic) SrIrO_3 in the U -SOC space (see Fig. 7). Most significantly, we observe that the non-collinear spin ordering is missing and the entire

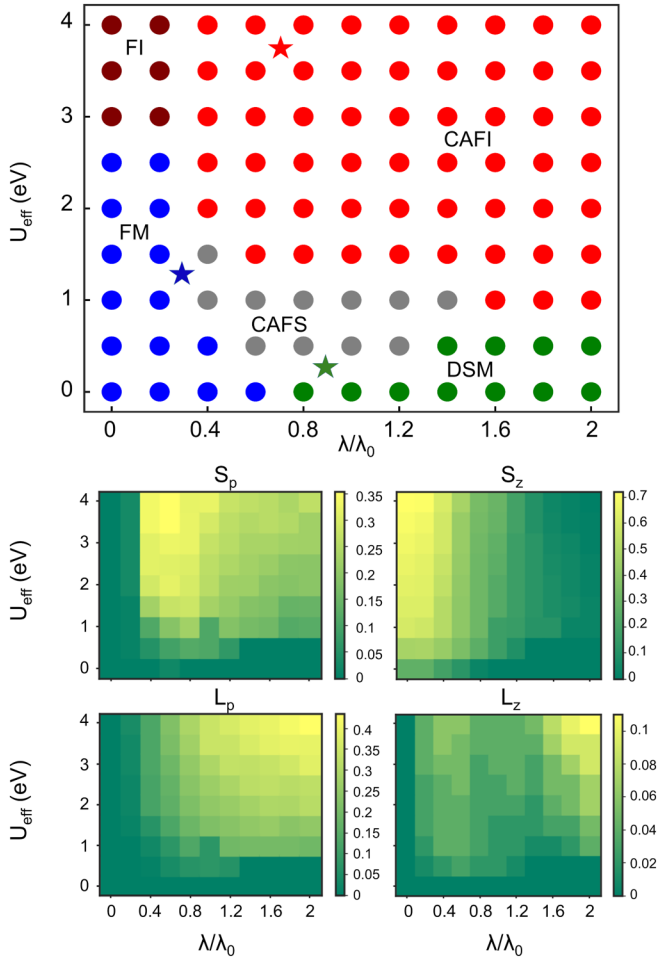


FIG. 5. (Top row) The electronic and magnetic phase diagram of orthorhombic SrIrO_3 as a function of U_{eff} and SOC. (Middle and bottom rows) The planar and normal component of spin moment (S_p and S_z) and orbital moment (L_p and L_z), respectively. The stars represent the ground state of LS d^5 perovskites. The green star represents CaIrO_3 , the blue star represents LaRuO_3 and SrRhO_3 , and the red star represents YRuO_3 , respectively.

phase diagram is spanned by collinear magnetic phases. There are four distinct phases observed and these are (i) FM, as shown in blue (ii) G-AFM, as shown in magenta, (iii) G-AFI, as shown in lime, and (iv) NM, as shown in cyan. In the weak SOC ($\lambda/\lambda_0 \leq 0.2$) and weak U_{eff} regime, the system

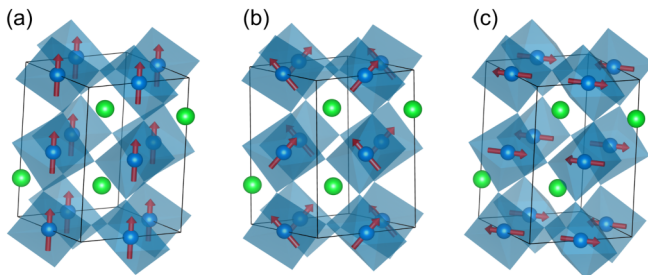


FIG. 6. Schematic illustrating evolution of magnetic ordering in bulk SrIrO_3 at $U_{\text{eff}} = 4$ eV with (a) $\lambda/\lambda_0 = 0$, (b) $\lambda/\lambda_0 = 1$, and (c) $\lambda/\lambda_0 = 2$, respectively.

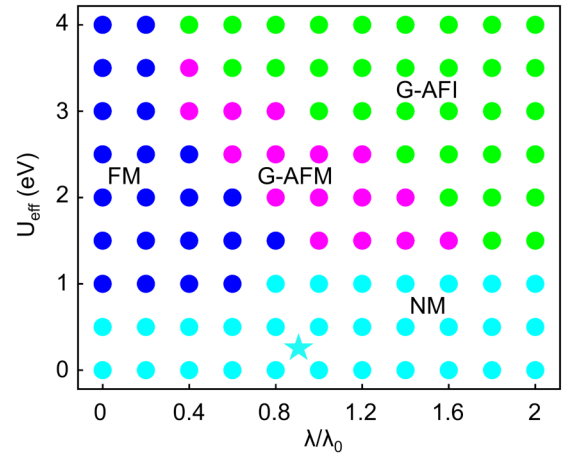


FIG. 7. The electronic and magnetic phase diagram of undistorted (cubic) SrIrO_3 as a function of U_{eff} and SOC. The star with cyan color represents the ground state of LS d^5 perovskite BaIrO_3 , respectively.

stabilizes in the NM state contrary to the FM phase, driven by small but finite moment, in the distorted structure. As the strength of on-site Coloumb repulsion increases, unlike the case of distorted structure, here no phase transition occurs and the system remains in the FM phase. The FM phase, for higher U_{eff} values, is well captured by our model Hamiltonian for the undistorted structure. In Appendix D, we have analyzed the orbital and spin resolved density of states (DOS) to show the robustness of the metallic phase for higher values of U_{eff} . For the intermediate SOC strength ($0.4 \leq \lambda/\lambda_0 \leq 1.6$), there is a narrow domain in which G-AFM phase stabilizes. In the strong U limit, transition from G-AFM to G-AFI phase occurs where the U_c value for metal-insulator transition is found to be high as compared to the distorted case. For example, U_c varies from 1 to 2 eV, whereas, for the undistorted case, a higher U_c between 2 to 4 eV is required for metal-insulator transition. The bandwidth, a measure of extent of localization, in a Hubbard model weakens the hopping integral roughly by a factor of $1/U$. The distortion also weakens the hopping integral. Therefore, the metal-insulator transition can be achieved with a lower value of U for the distorted structure. For the large SOC domain ($\lambda/\lambda_0 \geq 1.6$), the system exhibits either NM phase for lower U_{eff} values or G-AFI phase for intermediate and higher U_{eff} values. The compound BaIrO_3 [30], like SrIrO_3 , exhibits Pauli paramagnetic ground state and can be mapped to the region ($0.8 \leq \lambda/\lambda_0 \leq 1$, $0 \leq U \leq 1$ eV) in the phase diagram.

VI. ORIGIN OF NONCOLLINEAR MAGNETISM: EFFECT OF ROTATION AND TILTING

Absence of planar-spin component in the cubic SrIrO_3 implies that distortion is the key to the stabilization of non-collinear spin ordering. The effect of distortions on magnetic ordering is also observed in iridates and their superlattices. For example, $\text{Sr}_3\text{Ir}_2\text{O}_7$ exhibits a robust c -axis collinear antiferromagnetic ordering with negligible $\theta_r = 179.5^\circ$ [23,60] but on the other side, the bilayer superlattice 2SIO/1STO, exhibits c -axis canted AF ordering which is attributed to

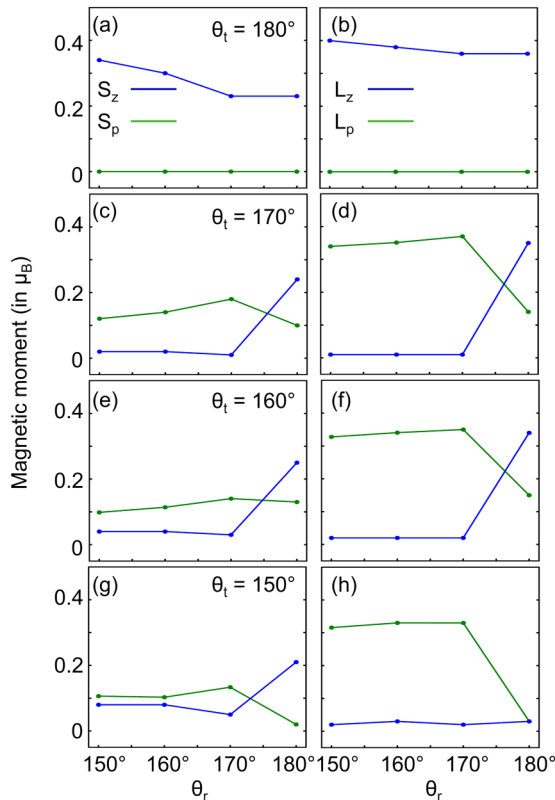


FIG. 8. Variation of planar and normal spin (first column) and orbital moments (second column) with rotation and tilting of octahedra, respectively.

the presence of finite θ_t ($\approx 172^\circ$). It has been reported that further enhancement of θ_t beyond 172° can even drive the 2SIO/ISTO through a quantum critical point where out-of-plane collinear to in-plane canted magnetic phase transition occurs [61]. Therefore, to analyze the effect of structural distortions on the LS state of d^5 perovskites, we have provided a quantitative measure of it by creating a geometrical design, described in Appendix B where the θ_r and θ_t can be varied smoothly.

For $\lambda/\lambda_0 = 1$ and $U_{\text{eff}} = 4$ eV, the planar and normal spin and orbital moments are plotted as a function of θ_r and θ_t in Fig. 8. In the absence of tilting, $\theta_t = 180^\circ$, see Figs. 8(a) and 8(b), the system always favors collinear spin ordering with vanishing S_p and L_p components. As far as S_z is concerned, it increases with θ_r for $\theta_t = 180^\circ$, hence, increasing the total magnetization of the system. Finite tilting [see Figs. 8(c), 8(e) and 8(g)] leads to a noncoplanar spin arrangement where S_z decreases sharply with increasing S_p component up to $\theta_r = 170^\circ$. With further increase in θ_r , S_p component decreases whereas S_z component increases and finally both components become comparable for higher values of θ_r . More or less the L_p component also follows the same trend as the S_p with increase in θ_r but with a magnitude larger as compare to the S_p [see Figs. 8(d), 8(f) and 8(h)]. However, for $\theta_t = 150^\circ$, the L_z component vanishes completely suggesting quenching of the L_z component for higher θ_t . The isospin reorientation with tilting and rotation that we get from this first-principles study is attributed to the orbital mixing hoppings arising in

the distorted frame. Many body models are being designed to relate such spin anisotropy to the Kitaev-type interactions developed due to octahedral tilting [58].

VII. SUMMARY AND OUTLOOK

To summarize, we developed a multiband model Hamiltonian and performed density functional calculations to study the electronic and magnetic structure of SrIrO₃ and examined the role of on-site Coulomb repulsion and spin-orbit coupling in the cubic and distorted structural framework. Furthermore, we used SrIrO₃ as a prototype to examine the electronic structure of low-spin d^5 perovskites in general by building a phase diagram and also smoothly varied the rotation and tilting of the IrO₆ octahedra to bring a third dimension into it. Our study reveals that there are eight quantum phases, namely, nonmagnetic metal, nonmagnetic Dirac semimetal, ferromagnetic metal, ferromagnetic insulator, G-type antiferromagnetic metal, G-type antiferromagnetic insulator, canted antiferromagnetic semimetal, and canted antiferromagnetic insulator as shown in Figs. 5 and 7 of the main text. The mechanism driving such phases are explained in detail. Further, we find that each of them form a soft boundary to allow a continuous phase transition from one phase to the other by varying the interaction strengths. The phase diagram is validated by mapping the ground state of the reported low-spin d^5 perovskites CaIrO₃, BaIrO₃, SrRhO₃, and YRuO₃ in the phase diagrams.

By scanning the periodic table, we see that low-spin d^5 transition metal oxide perovskites can be designed by exploring the following group combinations: I-X, II-IX, III-VIII (KPtO₃, RbPtO₃, MgRhO₃, ScRuO₃, ScOsO₃ and YO₃, etc.). Theoretically, the thermodynamical stability of such systems can be examined and experimental synthesis can be attempted with the advent of state of the art synthesis techniques such as atom by atom deposition methods and high pressure methods. Furthermore, the two formula unit double perovskite transition metal oxides with d^5 state can be thought of as sister members where similar competing interactions govern the system. In this way, the phases proposed in the phase diagram can be achieved. The interaction strengths can be varied under external stimuli such as pressure and strain, as well as through changing the chemical composition, design of heterostructures, etc. to induce quantum phase transition in these systems. As a whole, we believe that the present study will trigger experimental and theoretical studies to envisage novel quantum phases and applications.

ACKNOWLEDGMENTS

The authors thank HPCE, IIT Madras for providing the computational facility. This work is funded by the Department of Science and Technology, India, through Grant No. CRG/2020/004330.

APPENDIX A: TRANSFORMATION OF HOPPING MATRICES UNDER ROTATION AND TILTING OF OCTAHEDRA

In this Appendix we briefly explain the transformation of TB matrices for hopping between different sublattices under

rotation and tilting of octahedra. Distortion can be described in the form of octahedral rotation and tilting which varies from one Ir site to the another as shown in Fig. 1(a). Here, + or – signs on each Ir site indicates the clockwise or counterclockwise rotation and tilting of octahedra. The transformation of hopping matrices is determined by a site dependent 5×5 rotation matrix [Eq. (A4)] [62,63]. Denoting unrotated and rotated basis in the order $(xy, yz, xz, x^2-y^2, 3z^2-r^2)$ for the *A* sublattice as $|\alpha\rangle$ and $|\alpha'\rangle$, for the *B* sublattice as $|\beta\rangle$ and $|\beta'\rangle$, so that $|\alpha'\rangle = R |\alpha\rangle$ and $|\beta'\rangle = R' |\beta\rangle$, where *R* and *R'* are corresponding rotation matrices for the *A* and *B* sublattices, the hopping integral in the rotated basis is then given by

$$\tilde{H}_{\alpha',\beta'} = \langle \alpha' | H | \beta' \rangle = \langle \alpha | R^T H R' | \beta \rangle. \quad (\text{A1})$$

Hence, the Hamiltonian in the rotated basis is given by

$$\tilde{H} = R^T H R'. \quad (\text{A2})$$

The total rotation matrix for each site for Ir site can be described as the multiplication of two individual rotation and tilt matrices. The product is given by

$$R(\theta_r, \theta_t) = R(\theta_r)R(\theta_t), \quad (\text{A3})$$

where $R(\theta_r)$ denotes the pure rotation about the *z* axis, whereas $R(\theta_t)$ denotes the rotation about the crystal axis *a*. For pure rotation about the *z* axis, the Euler angles $(\alpha, \beta, \gamma) = (\theta_r, 0, 0)$, whereas for tilting $(\alpha, \beta, \gamma) = (-45^\circ, \theta_t, 45^\circ)$, respectively. Using these Euler angles, $R(\theta_r)$ and $R(\theta_t)$ can be obtained using *R* given by

$$R = \frac{1}{2} \begin{pmatrix} \beta'_+{}^2 \cos(2\alpha + 2\gamma)/2 & \beta'_+ \sin \beta \cos(2\alpha + \gamma) & \beta'_+ \sin \beta \sin(2\alpha + \gamma) & \beta'_+{}^2 \sin(2\alpha + 2\gamma)/2 & \sqrt{3} \sin^2 \beta \\ -\beta'_-{}^2 \cos(2\alpha - 2\gamma)/2 & +\beta'_- \sin \beta \cos(2\alpha - \gamma) & -\beta'_- \sin \beta \sin(2\alpha - \gamma) & +\beta'_-{}^2 \sin(2\alpha - 2\gamma)/2 & \sin 2\alpha \\ -\beta'_+ \sin \beta \cos(\alpha + 2\gamma) & \beta'_+ \beta''_- \cos(\alpha + \gamma) & \beta'_+ \beta''_- \sin(\alpha + \gamma) & -\beta'_+ \sin \beta \sin(\alpha + 2\gamma) & \sqrt{3} \sin \alpha \\ -\beta'_- \sin \beta \cos(\alpha - 2\gamma) & +\beta'_- \beta''_+ \cos(\alpha - \gamma) & -\beta'_- \beta''_+ \sin(\alpha - \gamma) & +\beta'_- \sin \beta \sin(\alpha - 2\gamma) & \sin 2\beta \\ \beta'_+ \sin \beta \sin(\alpha + 2\gamma) & -\beta'_+ \beta''_- \sin(\alpha + \gamma) & \beta'_+ \beta''_- \cos(\alpha + \gamma) & -\beta'_+ \sin \beta \cos(\alpha + 2\gamma) & \sqrt{3} \cos \alpha \\ +\beta'_- \sin \beta \sin(\alpha - 2\gamma) & -\beta'_- \beta''_+ \sin(\alpha - \gamma) & -\beta'_- \beta''_+ \cos(\alpha - \gamma) & +\beta'_- \sin \beta \cos(\alpha - 2\gamma) & \sin 2\beta \\ -\beta'_+{}^2 \sin(2\alpha + 2\gamma)/2 & -\beta'_+ \sin \beta \sin(2\alpha + \gamma) & \beta'_+ \sin \beta \cos(2\alpha + \gamma) & \beta'_+{}^2 \cos(2\alpha + 2\gamma)/2 & \sqrt{3} \sin^2 \beta \\ +\beta'_-{}^2 \sin(2\alpha - 2\gamma)/2 & -\beta'_- \sin \beta \sin(2\alpha - \gamma) & -\beta'_- \sin \beta \cos(2\alpha - \gamma) & \beta'_-{}^2 \cos(2\alpha - 2\gamma)/2 & \cos 2\alpha \\ -\sqrt{3} \sin^2 \beta \sin 2\gamma & \sqrt{3} \sin 2\beta \sin \gamma & -\sqrt{3} \sin 2\beta \cos \gamma & \sqrt{3} \sin^2 \beta \cos 2\gamma & 2 - 3 \sin^2 \beta \end{pmatrix}, \quad (\text{A4})$$

where $\beta'_\pm = 1 \pm \cos \beta$ and $\beta''_\pm = 2 \cos \beta \pm 1$.

In the rotated basis, the TB hopping matrices between *A* to *B* sublattice can be obtained by using the following equation:

$$\tilde{H}_{AB} = R^T(-\theta_r, -\theta_t) H_{AB} R(\theta_r, \theta_t) \quad (\text{A5})$$

where H_{AB} is the Hamiltonian in the unrotated basis. In compact form H_{AB} is expressed as

$$H_{AB} = \begin{pmatrix} H_{AB}^{\uparrow\uparrow} & H_{AB}^{\uparrow\downarrow} \\ H_{AB}^{\downarrow\uparrow} & H_{AB}^{\downarrow\downarrow} \end{pmatrix} \quad (\text{A6})$$

with $H_{AB}^{\uparrow\uparrow} = H_{AB}^{\downarrow\downarrow}$ and $H_{AB}^{\uparrow\downarrow} = H_{AB}^{\downarrow\uparrow} = 0$. The submatrix $H_{AB}^{\uparrow\uparrow}$ in the expanded form is given by

$$H_{AB}^{\uparrow\uparrow} = \begin{pmatrix} k_1 F_1 & 0 & 0 & 0 & 0 \\ 0 & k_2 F_1 & k_3 F_2 & 0 & 0 \\ 0 & k_3 F_2 & k_2 F_1 & 0 & 0 \\ 0 & 0 & 0 & k_4 F_1 & k_5 F_2 \\ 0 & 0 & 0 & k_5 F_2 & k_6 F_1 \end{pmatrix}, \quad (\text{A7})$$

where

$$\begin{aligned} F_1 &= \cos(k_x/2) \cos(k_y/2), \\ F_2 &= \sin(k_x/2) \sin(k_y/2), \\ k_1 &= 4t_1, \quad k_2 = 2t_1, \\ k_3 &= -2t_1, \quad k_4 = 3t_4, \\ k_5 &= \sqrt{3}t_4, \quad k_6 = t_4. \end{aligned} \quad (\text{A8})$$

Similarly, hopping between *A* to *A* sublattice is given by

$$\tilde{H}_{AA} = R^T(-\theta_r, -\theta_t) H_{AA} R(\theta_r, \theta_t), \quad (\text{A9})$$

where

$$H_{AA}^{\uparrow\uparrow} = \begin{pmatrix} k_7 F_3 & 0 & 0 & 0 & k_8 F_4 \\ 0 & k_9 F_6 & 0 & 0 & 0 \\ 0 & 0 & k_9 F_5 & 0 & 0 \\ 0 & 0 & 0 & k_{10} F_3 & 0 \\ k_8 F_4 & 0 & 0 & 0 & k_{11} F_3 \end{pmatrix}, \quad (\text{A10})$$

and the corresponding dispersions and hopping strength are given as

$$\begin{aligned}
 F_3 &= \cos k_x + \cos k_y, \\
 F_4 &= \cos k_x - \cos k_y, \\
 F_5 &= \cos k_x, \quad F_6 = \cos k_y, \\
 k_7 &= \frac{3}{2}t_2, \quad k_8 = -\frac{\sqrt{3}}{2}t_7, \\
 k_9 &= 2t_3, \quad k_{10} = 2t_6, \quad k_{11} = \frac{1}{2}t_5.
 \end{aligned} \tag{A11}$$

Similarly, the transformation and corresponding sublattice hopping matrices for interlayer coupling are given by

$$\tilde{H}_{AC} = R^T(-\theta_r, -\theta_t)H_{AC}R(-\theta_r, \theta_t), \tag{A12}$$

$$\tilde{H}_{AD} = R^T(-\theta_r, -\theta_t)H_{AD}R(\theta_r, \theta_t), \tag{A13}$$

$$H_{AC}^{\uparrow\uparrow} = \begin{pmatrix} 0 & 0 & 0 & 0 & 0 \\ 0 & k_{12}F_7 & 0 & 0 & 0 \\ 0 & 0 & k_{12}F_7 & 0 & 0 \\ 0 & 0 & 0 & 0 & 0 \\ 0 & 0 & 0 & 0 & k_{13}F_7 \end{pmatrix}, \tag{A14}$$

$$H_{AD}^{\uparrow\uparrow} = \begin{pmatrix} k_{14}F_8 & k_{15}F_{11} & k_{15}F_{10} & 0 & 0 \\ k_{15}F_{11} & k_{16}F_8 & k_{17}F_9 & k_{18}F_{10} & k_{19}F_{11} \\ k_{15}F_{10} & k_{17}F_9 & k_{16}F_8 & k_{18}F_{11} & k_{19}F_{10} \\ 0 & k_{18}F_{10} & k_{18}F_{11} & k_{20}F_8 & k_{21}F_9 \\ 0 & k_{19}F_{11} & k_{19}F_{10} & k_{21}F_9 & k_{22}F_8 \end{pmatrix}, \tag{A15}$$

and the corresponding dispersion relations and hopping strength are given as

$$\begin{aligned}
 F_7 &= \cos(k_z/2), \\
 F_8 &= \cos(k_x/2) \cos(k_y/2) \cos(k_z/2), \\
 F_9 &= \sin(k_x/2) \sin(k_y/2) \cos(k_z/2), \\
 F_{10} &= \sin(k_x/2) \sin(k_z/2) \cos(k_y/2), \\
 F_{11} &= \sin(k_y/2) \sin(k_z/2) \cos(k_x/2), \\
 k_{12} &= 2t_1, \quad k_{13} = 2t_4, \\
 k_{14} &= 4t_3, \quad k_{15} = -2\sqrt{2}t_3, \\
 k_{16} &= (3t_2 + 2t_3), \quad k_{17} = -(3t_2 - 2t_3), \\
 k_{18} &= -\frac{3}{\sqrt{2}}t_7, \quad k_{19} = -\sqrt{\frac{3}{2}}t_7, \\
 k_{20} &= \left(\frac{3}{2}t_5 + 2t_6\right), \quad k_{21} = (-\sqrt{3}t_5 + 2t_6), \\
 k_{22} &= \left(\frac{t_5}{2} + 6t_6\right).
 \end{aligned} \tag{A16}$$

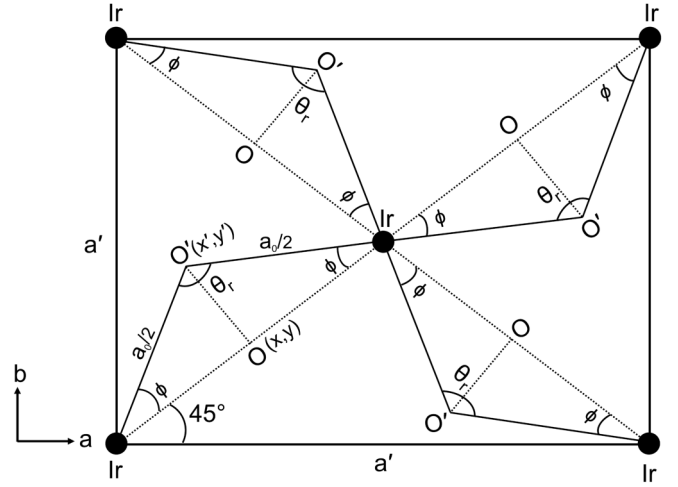


FIG. 9. Schematic illustration of geometrical design for inducing rotation in the ab plane. Here, a ($= \sqrt{2}a_0$) and a' are the lattice parameters of the undistorted and distorted structures, respectively.

APPENDIX B: GEOMETRICAL DESIGN FOR INDUCING ROTATION AND TILTING

The geometrical design for inducing rotation in the ab plane is shown in Fig. 9. This geometrical design differs from the equilibrium orthorhombic structure (see Fig. 10). For the former, the Ir-O bond lengths are uniform while the Ir-O-Ir bond-angles vary to facilitate the rotation and tilting. However, for the latter both bond-lengths and bond angles are anisotropic to minimize the energy. Therefore, this geometrical design can explicitly examine the effect of rotation and tilting on spin ordering. To do a quantitative measure

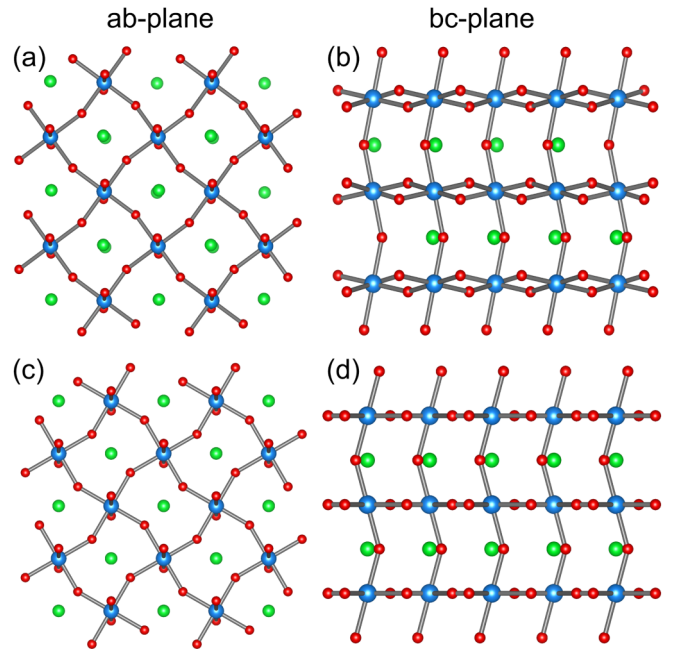


FIG. 10. Planar view of ab and bc planes for (a),(b) real orthorhombic structure, and (c),(d) for the designed supercell geometry.

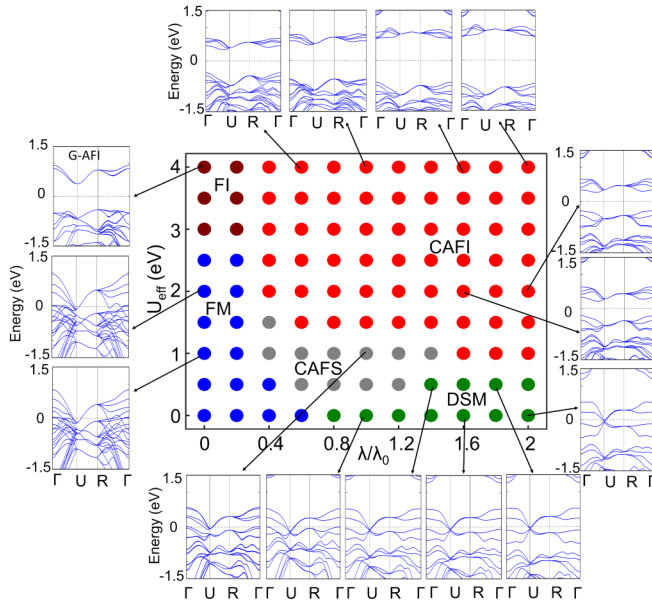


FIG. 11. Electronic band structures of CaIrO_3 marked on bulk phase diagram of SrIrO_3 for different values of U_{eff} and λ/λ_0 .

of it, we have specifically considered the case of bc plane tilting only. For analyzing the effect of structural distortions, a $\sqrt{2}a_0 \times \sqrt{2}a_0 \times 2a_0$ supercell is designed. Further distortion is induced in the supercell geometry by displacing the oxygen atoms in the ab (for rotation) as well in the bc (for tilting) plane keeping the Ir-O bond length fixed. The geometrical design for inducing rotation is shown in Fig. 9. For facilitating θ_r , oxygen atoms are displaced from their mean position $O(x,y)$ to $O'(x', y')$. In this process the lattice parameter changes from a to a' to maintain the constant bond length. By using similar geometry the tilting is designed in the bc plane. The lattice parameter for distorted structure and

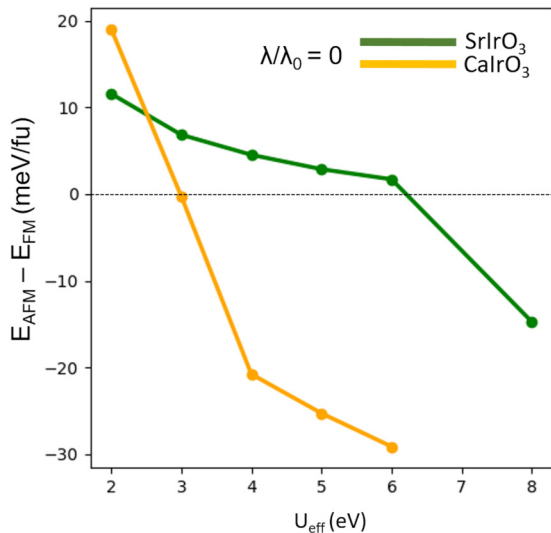


FIG. 12. Energy difference between G -type antiferromagnetic and ferromagnetic states as a function of U_{eff} for experimentally synthesized structures of SrIrO_3 and CaIrO_3 at $\lambda/\lambda_0 = 0$.

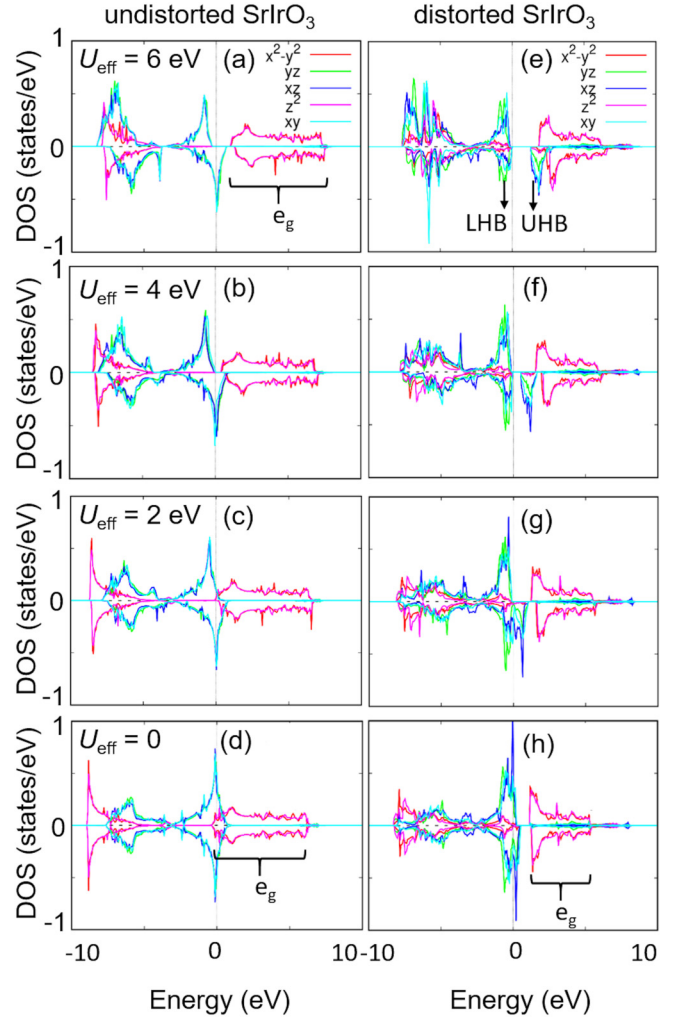


FIG. 13. Spin and orbital resolved density of states for undistorted (left column) and distorted SIO (right column) for $\lambda/\lambda_0 = 0$ and $U_{\text{eff}} = 0, 2, 4$ and 6 eV, respectively.

the coordinates of displaced oxygen atoms are related to each other by the following equations

$$x' = \frac{a' \cos(\phi + 45^\circ)}{2\sqrt{2} \cos \phi}, \quad (\text{B1})$$

$$y' = \frac{a' \sin(\phi + 45^\circ)}{2\sqrt{2} \cos \phi}, \quad (\text{B2})$$

$$a' = a \cos \phi. \quad (\text{B3})$$

APPENDIX C: COMPARISON BETWEEN BULK CaIrO_3 AND SrIrO_3

We have carried out calculations using the experimentally synthesized structure of CaIrO_3 [64] to examine the possible phases that this compound exhibits in the $U_{\text{eff}}-\lambda$ space. From the structural point of view CaIrO_3 and SrIrO_3 differ largely through tilting and rotation angles (θ_r and θ_t). For the former these are 153° and 156° while for the latter these are 141° and 143° .

For comparison, instead of replicating the full phase diagram of SIO (see Fig. 5) we have picked multiple points from each domain and calculated the electronic structure on these points to validate the acceptability of the phase diagram. The results are shown in Fig. 11. We indeed found the stabilization of five phases: FM, G-AFI, CAFS, CAFI, and DSM. The electronic structure of few selective points are marked on the bulk phase diagram of SIO and are shown in Fig. 11. The ground state DSM phase of CIO is very well captured (see the band structure in the bottom panel). Also, as seen in the case of SIO, the CAFI phase stabilizes for intermediate and higher values of λ/λ_0 and U_{eff} . Here, the boundaries of the phase diagrams should not be treated as hard boundaries and they might vary depending on the compound and due to different rotation and tilting angles. As can be seen from Fig. 12, in the case of CIO, we find that the system stabilizes in the G-AFI state beyond $U_{\text{eff}} = 3$ eV whereas for SIO the G-AFI state stabilizes beyond 6 eV. These G-AFI states are formed with low-spin d^5 states.

APPENDIX D: ROBUSTNESS OF THE CUBIC METALLIC PHASE

In Fig. 13, we have plotted the spin and orbital resolved DOS as a function of U_{eff} and for $\lambda/\lambda_0 = 0$. As can be clearly seen from the DOS of cubic (undistorted) SIO, for $U_{\text{eff}} = 0$, the e_g states are highly delocalized (bandwidth is ≈ 6 eV) and nearly unoccupied. For such states the role of on-site Coulomb repulsion U_{eff} is negligible which indeed is reflected for higher values of U_{eff} . In fact, with stronger U_{eff} , the e_g states are now completely unoccupied. As a result the system will always stabilize in a low-spin ($t_{2g}^5 e_g^0$) metallic state. When we introduce the experimentally observed distortions, reduced hopping decreases the bandwidth (see column 2 of Fig. 13). However, the e_g bandwidth is still large and there is a distortion induced bandgap which keeps the e_g states unoccupied. In this case increasing U_{eff} creates lower and upper Hubbard bands (LHB and UHB) out of the t_{2g} states and a new band gap emerges at the Fermi level [see Figs. 13(f) and 13(e)].

-
- [1] M. Z. Hasan and C. L. Kane, *Rev. Mod. Phys.* **82**, 3045 (2010).
- [2] X.-L. Qi and S.-C. Zhang, *Rev. Mod. Phys.* **83**, 1057 (2011).
- [3] D. Pesin and L. Balents, *Nat. Phys.* **6**, 376 (2010).
- [4] E. J. Bergholtz and Z. Liu, *Int. J. Mod. Phys. B* **27**, 1330017 (2013).
- [5] G. Baskaran, S. Mandal, and R. Shankar, *Phys. Rev. Lett.* **98**, 247201 (2007).
- [6] H. Takagi, T. Takayama, G. Jackeli, G. Khaliullin, and S. E. Nagler, *Nat. Rev. Phys.* **1**, 264 (2019).
- [7] Y. Okamoto, M. Nohara, H. Aruga-Katori, and H. Takagi, *Phys. Rev. Lett.* **99**, 137207 (2007).
- [8] B. Yan and C. Felser, *Annu. Rev. Condens. Matter Phys.* **8**, 337 (2017).
- [9] O. Vafek and A. Vishwanath, *Annu. Rev. Condens. Matter Phys.* **5**, 83 (2014).
- [10] X. Wan, A. Vishwanath, and S. Y. Savrasov, *Phys. Rev. Lett.* **108**, 146601 (2012).
- [11] X. Wan, A. M. Turner, A. Vishwanath, and S. Y. Savrasov, *Phys. Rev. B* **83**, 205101 (2011).
- [12] W. Witczak-Krempa, A. Go, and Y. B. Kim, *Phys. Rev. B* **87**, 155101 (2013).
- [13] G. E. Topp, N. Tancogne-Dejean, A. F. Kemper, A. Rubio, and M. A. Sentef, *Nat. Commun.* **9**, 4452 (2018).
- [14] J. G. Rau, E. K.-H. Lee, and H.-Y. Kee, *Phys. Rev. Lett.* **112**, 077204 (2014).
- [15] J. c. v. Chaloupka, G. Jackeli, and G. Khaliullin, *Phys. Rev. Lett.* **110**, 097204 (2013).
- [16] J. Reuther, R. Thomale, and S. Rachel, *Phys. Rev. B* **90**, 100405(R) (2014).
- [17] S. K. Takahashi, J. Wang, A. Arsenault, T. Imai, M. Abramchuk, F. Tafti, and P. M. Singer, *Phys. Rev. X* **9**, 031047 (2019).
- [18] E. M. Kenney, C. U. Segre, W. Lafargue-Dit-Hauret, O. I. Lebedev, M. Abramchuk, A. Berlie, S. P. Cottrell, G. Simutis, F. Bahrami, N. E. Mordvinova, G. Fabbris, J. L. McChesney, D. Haskel, X. Rocquefelte, M. J. Graf, and F. Tafti, *Phys. Rev. B* **100**, 094418 (2019).
- [19] M. Nauman, Y. Hong, T. Hussain, M. S. Seo, S. Y. Park, N. Lee, Y. J. Choi, W. Kang, and Y. Jo, *Phys. Rev. B* **96**, 155102 (2017).
- [20] B. J. Kim, H. Jin, S. J. Moon, J.-Y. Kim, B.-G. Park, C. S. Leem, J. Yu, T. W. Noh, C. Kim, S.-J. Oh, J.-H. Park, V. Durairaj, G. Cao, and E. Rotenberg, *Phys. Rev. Lett.* **101**, 076402 (2008).
- [21] H. Watanabe, T. Shirakawa, and S. Yunoki, *Phys. Rev. Lett.* **110**, 027002 (2013).
- [22] Y. J. Yan, M. Q. Ren, H. C. Xu, B. P. Xie, R. Tao, H. Y. Choi, N. Lee, Y. J. Choi, T. Zhang, and D. L. Feng, *Phys. Rev. X* **5**, 041018 (2015).
- [23] S. Fujiyama, K. Ohashi, H. Ohsumi, K. Sugimoto, T. Takayama, T. Komesu, M. Takata, T. Arima, and H. Takagi, *Phys. Rev. B* **86**, 174414 (2012).
- [24] Y. Chen, Y.-M. Lu, and H.-Y. Kee, *Nat. Commun.* **6**, 6593 (2015).
- [25] Y. F. Nie, P. D. C. King, C. H. Kim, M. Uchida, H. I. Wei, B. D. Faeth, J. P. Ruf, J. P. C. Ruff, L. Xie, X. Pan, C. J. Fennie, D. G. Schlom, and K. M. Shen, *Phys. Rev. Lett.* **114**, 016401 (2015).
- [26] J. Fujioka, T. Okawa, A. Yamamoto, and Y. Tokura, *Phys. Rev. B* **95**, 121102(R) (2017).
- [27] J. Fujioka, R. Yamada, M. Kawamura, S. Sakai, M. Hirayama, R. Arita, T. Okawa, D. Hashizume, M. Hoshino, and Y. Tokura, *Nat. Commun.* **10**, 362 (2019).
- [28] J. Fujioka, R. Yamada, T. Okawa, and Y. Tokura, *Phys. Rev. B* **103**, L041109 (2021).
- [29] J.-M. Carter, V. V. Shankar, M. A. Zeb, and H.-Y. Kee, *Phys. Rev. B* **85**, 115105 (2012).
- [30] J.-G. Cheng, T. Ishii, H. Kojitani, K. Matsubayashi, A. Matsuo, X. Li, Y. Shirako, J.-S. Zhou, J. B. Goodenough, C. Q. Jin, M. Akaogi, and Y. Uwatoko, *Phys. Rev. B* **88**, 205114 (2013).
- [31] H. Xia, J. Dai, Y. Xu, Y. Yin, X. Wang, Z. Liu, M. Liu, M. A. McGuire, X. Li, Z. Li, C. Jin, Y. Yang, J. Zhou, and Y. Long, *Phys. Rev. Mater.* **1**, 024406 (2017).
- [32] S. Mathi Jaya, R. Jagadish, R. S. Rao, and R. Asokamani, *Phys. Rev. B* **43**, 13274 (1991).
- [33] D. J. Singh, *Phys. Rev. B* **67**, 054507 (2003).

- [34] K. Ji, A. Paul, E. Solana-Madruga, A. M. Arevalo-Lopez, U. V. Waghmare, and J. P. Attfield, *Phys. Rev. Mater.* **4**, 091402(R) (2020).
- [35] M. A. Zeb and H.-Y. Kee, *Phys. Rev. B* **86**, 085149 (2012).
- [36] J. B. Torrance, P. Lacorre, A. I. Nazzal, E. J. Ansaldo, and C. Niedermayer, *Phys. Rev. B* **45**, 8209 (1992).
- [37] J. L. García-Muñoz, J. Rodríguez-Carvajal, P. Lacorre, and J. B. Torrance, *Phys. Rev. B* **46**, 4414 (1992).
- [38] S. Miyasaka, Y. Okimoto, M. Iwama, and Y. Tokura, *Phys. Rev. B* **68**, 100406(R) (2003).
- [39] J.-S. Zhou, J.-Q. Yan, and J. B. Goodenough, *Phys. Rev. B* **71**, 220103(R) (2005).
- [40] J.-S. Zhou, J. A. Alonso, V. Pomjakushin, J. B. Goodenough, Y. Ren, J.-Q. Yan, and J.-G. Cheng, *Phys. Rev. B* **81**, 214115 (2010).
- [41] T. Vogt, J. A. Hriljac, N. C. Hyatt, and P. Woodward, *Phys. Rev. B* **67**, 140401(R) (2003).
- [42] B. Kim, P. Liu, and C. Franchini, *Phys. Rev. B* **95**, 115111 (2017).
- [43] P. Liu, S. Khmelevskiy, B. Kim, M. Marsman, D. Li, X.-Q. Chen, D. D. Sarma, G. Kresse, and C. Franchini, *Phys. Rev. B* **92**, 054428 (2015).
- [44] J. G. Zhao, L. X. Yang, Y. Yu, F. Y. Li, R. C. Yu, Z. Fang, L. C. Chen, and C. Q. Jin, *J. Appl. Phys.* **103**, 103706 (2008).
- [45] G. Kresse and D. Joubert, *Phys. Rev. B* **59**, 1758 (1999).
- [46] P. E. Blöchl, *Phys. Rev. B* **50**, 17953 (1994).
- [47] G. Kresse and J. Furthmüller, *Phys. Rev. B* **54**, 11169 (1996).
- [48] S. L. Dudarev, G. A. Botton, S. Y. Savrasov, C. J. Humphreys, and A. P. Sutton, *Phys. Rev. B* **57**, 1505 (1998).
- [49] J. Longo, J. Kafalas, and R. Arnott, *J. Solid State Chem.* **3**, 174 (1971).
- [50] K. A. Modic, T. E. Smidt, I. Kimchi, N. P. Breznay, A. Biffin, S. Choi, R. D. Johnson, R. Coldea, P. Watkins-Curry, G. T. McCandless, J. Y. Chan, F. Gandara, Z. Islam, A. Vishwanath, A. Shekhter, R. D. McDonald, and J. G. Analytis, *Nat. Commun.* **5**, 4203 (2014).
- [51] S. Boseggia, R. Springell, H. C. Walker, H. M. Rønnow, C. Rüegg, H. Okabe, M. Isobe, R. S. Perry, S. P. Collins, and D. F. McMorrow, *Phys. Rev. Lett.* **110**, 117207 (2013).
- [52] J. Chaloupka and G. Khaliullin, *Phys. Rev. B* **94**, 064435 (2016).
- [53] A. Biffin, R. D. Johnson, I. Kimchi, R. Morris, A. Bombardi, J. G. Analytis, A. Vishwanath, and R. Coldea, *Phys. Rev. Lett.* **113**, 197201 (2014).
- [54] J. C. Slater and G. F. Koster, *Phys. Rev.* **94**, 1498 (1954).
- [55] Q. Luo, Numerical study of hubbard model for iron-based superconductors, Ph.D. thesis, University of Tennessee, 2013.
- [56] J. Kanamori, *Prog. Theor. Phys.* **30**, 275 (1963).
- [57] O. N. Meetei, W. S. Cole, M. Randeria, and N. Trivedi, *Phys. Rev. B* **91**, 054412 (2015).
- [58] S. Mohapatra, S. Aditya, R. Mukherjee, and A. Singh, *Phys. Rev. B* **100**, 140409(R) (2019).
- [59] H. Kobayashi, M. Nagata, R. Kanno, and Y. Kawamoto, *Mater. Res. Bull.* **29**, 1271 (1994).
- [60] T. Hogan, L. Bjaalie, L. Zhao, C. Belvin, X. Wang, C. G. Van de Walle, D. Hsieh, and S. D. Wilson, *Phys. Rev. B* **93**, 134110 (2016).
- [61] D. Meyers, Y. Cao, G. Fabbris, N. J. Robinson, L. Hao, C. Frederick, N. Traynor, J. Yang, J. Lin, M. H. Upton, D. Casa, J.-W. Kim, T. Gog, E. Karapetrova, Y. Choi, D. Haskel, P. J. Ryan, L. Horak, X. Liu, J. Liu *et al.*, *Sci. Rep.* **9**, 4263 (2019).
- [62] S. Mohapatra, C. Bhandari, S. Satpathy, and A. Singh, *Phys. Rev. B* **97**, 155154 (2018).
- [63] M. Tinkham, *Group Theory and Quantum Mechanics* (McGraw-Hill, New York, 1964).
- [64] T. Tsuchiya and J. Tsuchiya, *Phys. Rev. B* **76**, 144119 (2007).